Received: 20 August 2021 | Revised: 22 December 2021 | Accepted: 18 January 2022

DOI: 10.1111/jon.12975

JOURNAL OF NEUROIMAGING
THE OFFICIAL JOURNAL OF THE AMERICAN SOCIETY OF NEUROIMAGING
WILEY

CLINICAL INVESTIGATIVE STUDY

Comparison of MRI methods for measuring whole-brain oxygen extraction fraction under different geometric conditions at 7T

Anna Lundberg[1] | Emelie Lind[1] | Hampus Olsson[1] | Gunther Helms[1] | Linda Knutsson[1,2] | Ronnie Wirestam[1]

[1] Department of Medical Radiation Physics, Lund University, Lund, Sweden

[2] Russell H. Morgan Department of Radiology and Radiological Science, Johns Hopkins University School of Medicine, Baltimore, Maryland, United States

Correspondence
Ronnie Wirestam, Department of Medical Radiation Physics, Lund University, Skåne University Hospital, SE-22185 Lund, Sweden.
Email: ronnie.wirestam@med.lu.se

Funding information
This study was supported by the Swedish Research Council (MH 2017-00995 and NT 2014-6193) and Hjärnfonden (grant no. FO2018-0145).

Abstract

Background and Purpose: Cerebral tissue oxygenation is a critical brain viability parameter, and the magnetic properties of hemoglobin offer the opportunity to noninvasively quantify oxygen extraction fraction (OEF) by magnetic resonance imaging (MRI). Ultrahigh-field MRI shows advantages such as increased sensitivity to magnetic susceptibility differences and improved signal-to-noise ratio that can be translated into smaller voxel size, but also increased sensitivity to static and B1 field inhomogeneities. The aim was to produce a systematic comparison of three MRI-based methods for estimation of OEF.

Methods: OEF estimates in 16 healthy subjects were obtained at 7T utilizing susceptometry-based oximetry (SBO), quantitative susceptibility mapping (QSM), and transverse relaxation rate (R2*). Two major draining veins, that is, the superior sagittal sinus (SSS) and the straight sinus (SS), were investigated, including mutual agreement between the methods in each of the two different vessels, agreement between vessels as well as potential vessel angle and vessel size dependences.

Results: Very good correlation ($r = .88$) was found between SBO-based and QSM-based OEF estimates in SSS. Only QSM showed a moderate correlation ($r = .61$) between corresponding OEF estimates in SSS and SS. For SBO, a trend of increasing OEF estimates was observed as the SS vessel angle relative to the main magnetic field increased. No obvious size dependence could be established for any method. The R2*-based OEF estimates were reasonable (35%-36%), but the observed range was somewhat low.

Conclusion: The results indicate that QSM is a promising candidate for assessment of OEF estimates, for example, providing reasonably robust estimates across a wide range of vessel orientations.

KEYWORDS
cerebral hemodynamics, cerebral oxygenation, magnetic resonance imaging, quantitative susceptibility mapping, R2* mapping, susceptometry-based oximetry, venous oxygen saturation

INTRODUCTION

Despite the vital requirement of oxygen, the internal oxygen reserves in brain tissue are limited and cerebral oxygen metabolism relies upon a delicate coupling between cerebral blood flow (CBF) and the oxygen extraction fraction (OEF), that is, the fractional amount of oxygen extracted by brain parenchyma during the passage through the microvasculature.[1] Impaired CBF, for instance under ischemic conditions, is accompanied by a compensatory increase in OEF to ensure normal neuronal activity. Permanent brain damage may emerge if oxygen supply, regardless of the elevated OEF, becomes insufficient to maintain the required oxygen metabolism.[2] Reliable quantification of brain oxygenation would not only improve the understanding of healthy cerebral physiology but also be of clinical relevance in several conditions such as stroke, tumors, or neurodegenerative disorders.[1] Furthermore, OEF has proven to serve as an important biomarker for tissue viability, and elevated OEF can support identification of the ischemic penumbra in acute ischemic stroke and guide treatment of disease.[3]

Established OEF methods include, for example, jugular venous oximetry[4] and near-infrared spectroscopy.[5] The former technique provides only global oxygenation values, and is still of limited potential for routine use, whereas the latter method is inherently limited to regions near the skull surface. The gold standard method for OEF mapping in vivo is generally considered to be ^{15}O PET,[6] but clinical implementations are still limited, because the PET technique is associated with relatively low spatial resolution, administration of short half-life tracers, and considerable radiation exposure that hampers repeated studies.

Several MRI methods for noninvasive assessment of the deoxyhemoglobin (dHb) content and for quantification of venous oxygen saturation have also been developed, based primarily on the strongly paramagnetic effect displayed by dHb.[7]

First, dHb shows various effects on the transverse relaxation of blood and surrounding parenchyma. The paramagnetic dHb creates magnetic field gradients in the vicinity of red blood cells, implying that transverse relaxation is strongly dependent on the concentration of dHb.[8,9] Calibration curves of blood transverse relaxation time versus oxygen saturation level have been experimentally established in vitro,[10,11] and, in its simplest concept, OEF can be estimated by measuring $T2^* = 1/R2^*$ and employing such a calibration curve. More intricate OEF methods include the T2*-based calibrated blood-oxygenation-level-dependent (BOLD) technique,[12] as well as the quantitative BOLD technique[13] using $R2'$-weighted data (where $R2' = 1/T2^* - 1/T2$) in combination with complex modeling relating the relaxation rate to the dHb concentration. T2-relaxation-under-spin-tagging[14] utilizes spin labeling theory for labeling blood in larger terminal veins, enabling T2 to be determined in large veins and converted to global OEF using a calibration curve.

Second, the dHb concentration scales linearly with blood magnetic susceptibility.[15] In susceptometry-based oximetry (SBO), blood oxygen saturation and OEF in major vessels, modeled as paramagnetic cylinders, can be obtained by measuring the resulting phase shift.[16–20] The method is well-established and robust for global venous oxygen saturation in the largest cerebral venous draining vessel, that is, the superior sagittal sinus (SSS).[21] Being relatively long and straight, the SSS makes a suitable candidate for the required infinite cylinder approximation, and it exhibits a venous oxygen saturation almost identical to that in the internal jugular vein.[22,23] However, errors in SBO estimates can arise from vessel tilt and curvature, vessel cross sections being noncircular, and from induced magnetic field gradients,[19,24–26] and only medium-sized to large vessels with appropriate geometry can be analyzed. Fan et al.[27] proposed an extension of the technique to smaller veins with advantageous orientations, but also suggested proceeding toward using quantitative susceptibility mapping (QSM).

The QSM technique allows for oxygen saturation to be quantified more generally, in veins of arbitrary orientation and geometry. The underlying susceptibility distribution is reconstructed from the measured magnetic field inhomogeneities resulting from the susceptibility sources.[28–32] Several studies have demonstrated its potential for quantitative blood oxygenation measurements.[33–37] Fan et al.[34] used large- and medium-sized veins in the obtained QSM map to construct a three-dimensional venogram with superimposed oxygen saturation values along the venous vessel tree, and good correlation between QSM and PET has been reported regarding identification of elevated OEF levels.[36,37] The QSM reconstruction process is, however, mathematically challenging and still not fully robust.[1,32] Critical steps in the postprocessing include selection of a suitable brain mask[38] and separation between background field and local tissue field.[39] Furthermore, QSM accuracy at different in vivo oxygenation levels and geometric conditions needs to be established. Hence, validations and systematic comparisons are required to allow progression toward clinical implementation.

In summary, MRI, being inherently sensitive to dHb, is a promising candidate for robust quantification of brain oxygen extraction with sufficient spatial resolution, and 7T shows additional advantages in terms of enhanced sensitivity to susceptibility effects and high signal-to-noise ratio that can be translated into smaller voxel size. Although some previous studies have dealt with comparing different MRI techniques,[21,34,40,41] a systematic investigation of mutual agreement is still warranted. Hence, the aim of this study was to conduct a systematic comparison of three OEF methods, based on R2*, SBO, and QSM, in the same cohort of healthy subjects at 7T. As a reasonable starting point for evaluation, the study focused on larger vessels and global OEF. Resting-state OEF was compared under simple geometrical conditions in SSS and under somewhat more challenging geometric circumstances in the straight sinus (SS).

METHODS

Theory

Magnetic susceptibility information from MRI phase images

When exposed to an external magnetic field, the underlying susceptibility distribution $\chi(r)$ of the tissue introduces an intricate and

nonlocal magnetic field perturbation. The corresponding phase shift $\Delta\emptyset(r)$ is given by[42]

$$\Delta\emptyset(r) = \gamma \cdot B_0 \cdot \Delta TE \cdot d \otimes \chi(r), \quad (1)$$

where r is the voxel position given in spherical coordinates, γ is the proton gyromagnetic ratio, B_0 is the magnetic flux density of the main magnetic field, ΔTE is the echo time difference in multi-echo gradient echo acquisitions, and $d = \frac{3\cos^2\vartheta - 1}{4\pi r^3}$ is the z-component of the unit dipole kernel (ϑ is the observation angle relative to the main magnetic field). The inversion required to obtain the spatial susceptibility from measured phase is ill-posed,[42] and the estimation of magnetic susceptibility from phase images is referred to as QSM.[28–32] However, for certain simple geometric conditions an analytical solution can be derived, as used in SBO. If the vein of interest is modeled as a cylinder with length >> diameter and the angle ϑ relative to the main magnetic field, the manifested phase difference $\Delta\Phi$ between the surrounding tissue and the venous vessel can be expressed as[18]

$$\Delta\Phi = \gamma \cdot \frac{1}{6} \cdot \Delta\chi \cdot B_0 \cdot (3\cos^2\vartheta - 1) \cdot \Delta TE, \quad (2)$$

where $\Delta\chi$ is the susceptibility difference between the surrounding tissue (here assumed to represent arterial blood) and the venous vessel.

Estimation of OEF

If the arterial oxygen saturation is assumed to be 100%, OEF can be expressed as $OEF = 1 - Y$, where Y is the fractional venous oxygen saturation level, and the relationship between OEF and the susceptibility difference $\Delta\chi$ is given by[16]

$$\Delta\chi = \Delta\chi_{do} \cdot Hct \cdot OEF, \quad (3)$$

where $\Delta\chi_{do} = 0.27 \cdot 4\pi$ ppm (in SI units) is the susceptibility difference per unit hematocrit between fully deoxygenated and fully oxygenated blood,[43,44] and $Hct = 0.4$ is the assumed fractional hematocrit.[45] Hence, Equation (3) enables estimation of OEF using QSM-based susceptibility estimates. Furthermore, if the vein of interest is modeled as an infinite cylinder, a combination of Equations (2) and (3) allows OEF to be calculated from the estimated local phase according to

$$OEF = \frac{\Delta\Phi \cdot 6}{\gamma \cdot \Delta\chi_{do} \cdot Hct \cdot B_0 \cdot (3\cos^2\vartheta - 1) \cdot \Delta TE}. \quad (4)$$

OEF assessment based on R2* information can be obtained using the following mathematical representation of a 7T calibration curve relating venous R2* to dHb content and Y (at $Hct = 0.435$), established by Blockley et al.[11] (Blockley, personal communication):

$$R2^* = 75.2 + 832\,(OEF)^2 \ [s^{-1}]. \quad (5)$$

MRI data acquisition

The study was approved by the regional Ethical Review Board, and informed written consent was obtained from each participant before the investigation. In total, 16 healthy volunteers (9 males, 7 females, age range 25-52 years) participated in the study. All data were acquired using an actively shielded 7T MR system (Achieva, Philips Healthcare, Best, NL), equipped with a two-channel transmit/32-channel receive head coil (Nova Medical, Wilmington, MA). A nonselective 3-dimensional multiparametric mapping protocol based on a multi-echo RF-spoiled gradient echo sequence was used for T1-weighted (T1-W) and PD-weighted (PD-W) acquisitions,[46] subsequently used to extract phase, QSM, and R2* data. The flip angle was 16° for the T1-W images and 4° for PD-W images, and volumes were acquired with a field of view of 230 × 230 mm^2 in the sagittal plane and a slab thickness of 200 mm in the right-left direction (with small variations due to different subject sizes) corresponding to an isotropic voxel size of 0.9 × 0.9 × 0.9 mm^3. Readout was set to be in the head-feet direction and the readout gradient polarity was alternated to reduce gradient heating, eddy currents, and peripheral nerve stimulation. Images at eight equidistant echo times (TEs) at multiples of 1.97 ms were acquired, without internal linear correction, within a repetition time of 18 ms. A SENSE factor = 2 was used in both phase-encoding directions and, with elliptical k-space filling, the scan time was 3 min and 23 s. Small variations in protocol parameters existed in some cases, but had no significant impact on the further analysis.

Image processing

Phase and QSM maps were obtained from collected T1-W multi-echo phase and magnitude data, using a software package including the morphology-enabled dipole inversion (MEDI) algorithm (Cornell University, https://pre.weill.cornell.edu/mri/pages/qsm.html).[31,42,47,48] In brief, phase images corresponding to ΔTE were generated from the magnetic field shift estimated using a nonlinear least-square fitting to measured complex data.[48–50] Thereafter, spatial phase unwrapping was performed using the Laplacian method,[51] followed by background field removal using a projection onto dipole field (PDF) method,[52] in order to extract the phase map that corresponds to the local field distribution. Finally, these obtained phase maps were used for the SBO method and as input into the MEDI algorithm for reconstruction of the QSM maps. In the solution of the inverse problem (cf. Equation 1) using MEDI, a regularization parameter λ needs to be optimized with respect to accurate quantification of the magnetic susceptibility and thus also of the OEF.

For the R2*-based OEF measurements, R2* maps were generated by the hMRI toolbox,[53] using a simultaneous optimized log-linear fit of the T1-W and PD-W multi-echo data, as described in detail by Weiskopf et al.[54] The method, denoted ESTATICS, enables robust R2* estimates with less sensitivity to motion-related artifacts and higher SNR compared to R2* maps generated from only a single contrast weighting.

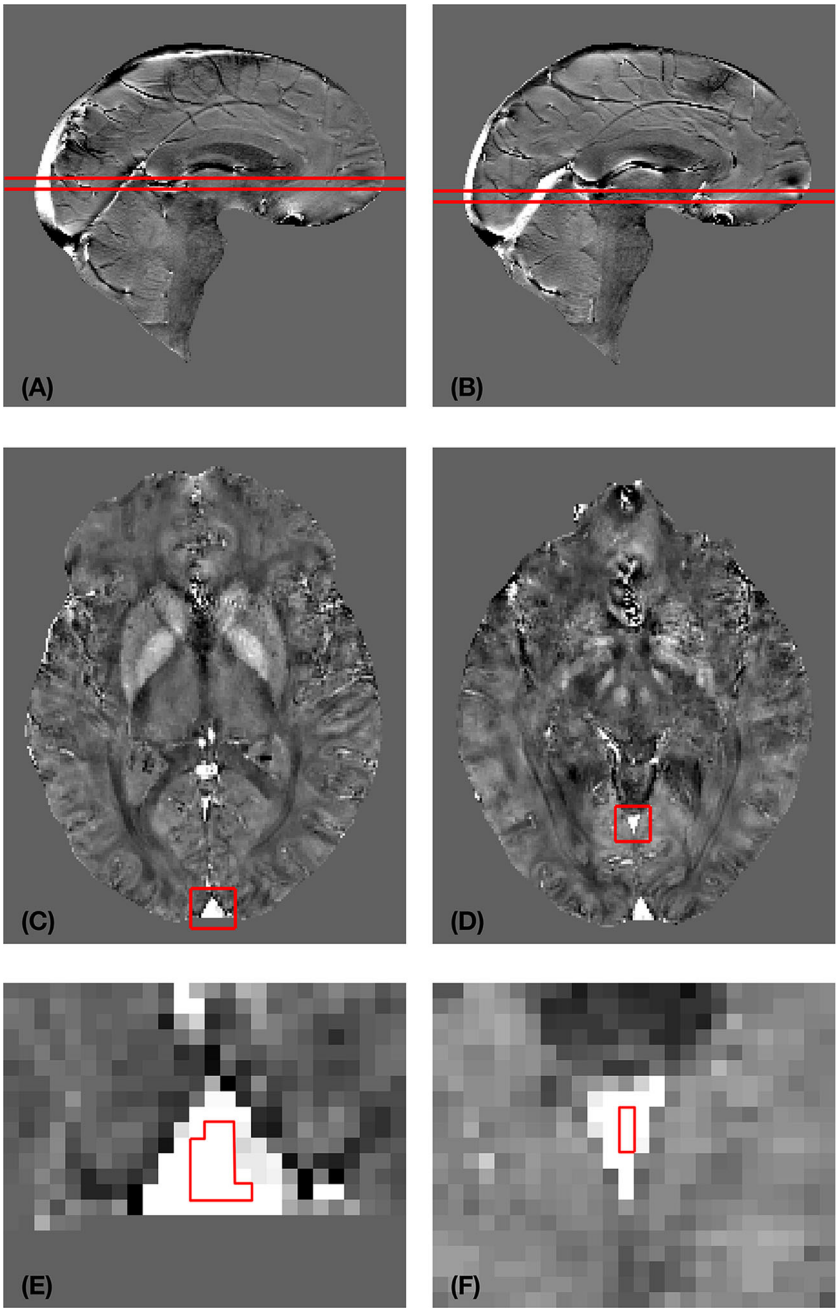

FIGURE 1 Selected slab of interest (SOI) delimited by red lines for (A) superior sagittal sinus (SSS) and (B) straight sinus (SS). Selected volume of interest (indicated by red rectangle) for (C) SSS and (D) SS in one slice of the SOI for one volunteer. The corresponding region of interest delineation (in red) in the same slice, used for the percentile-based value selection, is shown for (E) SSS and (F) SS

Data analysis

For measurements using all three OEF methods (ie, SBO, QSM, and R2*), values for venous blood need to be estimated. The voxels representing venous blood were defined using the procedures described below and two different vessels (SSS and SS) were then analyzed.

Initially, a slab of interest (SOI) consisting of six consecutive slices (Figure 1A,B) was manually identified for each volunteer and for each type of vessel (SSS and SS), characterized by lack of major artifacts interfering with relevant structures (in any of the QSM, phase, or R2* datasets), while at the same time including the vessel of interest located at a position suitable for the infinite cylinder approximation in combination with either an angle close to being parallel with the main magnetic field (when measuring in the SSS) or with a stable and well-defined angle (when measuring in the SS).

In each SOI, smaller volumes of interest (VOIs) (approximately $13 \times 13 \times 5$ mm^3), mainly covering the vessel of interest (Figure 1C,D), were chosen and applied to images corresponding to the three different datasets. The venous vessel of interest was obtained through segmentation of the VOI venous voxels using a venous mask, defining venous values as all values larger than the mean +2 standard deviations (mean + 2SDs) of the corresponding SOI values, similarly to previously described approaches.[36,55] In order to investigate the variability introduced by different approaches for identifying the "partial

TABLE 1 Selected percentiles of the venous vessel values

Percentiles used		
Vessel type	**QSM/SBO**	**R2***
SSS	71st	62nd
SS	81st	76th

Note: Selected percentiles applied to the venous values in the volume of interest, after application of the venous vessel mask, for the different methods, that is, quantitative susceptibility mapping (QSM), susceptometry-based oximetry (SBO), and transverse relaxation rate (R2*), and the different vessel types, that is, superior sagittal sinus (SSS) and straight sinus (SS).

volume effects (PVE)-free venous values" (ie, the values assumed not to be affected by partial volume effects), this step was followed by either (i) averaging of the 5%-50% highest values within the vessel (ie, different thresholds were investigated as further described below) or (ii) by a percentile-based (PB) value selection, described below and specified in Table 1, for the different methods and vessel types (ie, SSS and SS).

An automated method for extracting the PVE-free venous values is important to eliminate operator-induced bias, but it is also of interest to establish how an approach based on manual ROI selection compares to automated routines. Hence, in a subset of the volunteers, R2*-, phase-, and QSM-based susceptibility mean values in SSS and SS were extracted from manually selected regions of interest (ROIs), covering mainly central voxels of the vein of interest (Figure 1E,F) in the SOI. The percentiles chosen in case (ii), after application of the venous mask, were selected to match, as closely as possible, the corresponding manually obtained mean values (Table 1).

For estimation of OEF using SBO and the QSM-based method, values representing the surrounding tissue are also needed. Thus, the mean values of the SOI, after exclusion of venous voxels, in the phase and QSM maps, were used to represent the phase and susceptibility value, respectively, of the surrounding tissue.

The SBO method also requires the vessel orientation relative to the B_0 direction. Hence, each vessel of interest was displayed and analyzed in the three principal anatomical planes (see Figure 2), and the sagittal plane was used to estimate the vessel angle using an angle measurement tool in the image processing software (ImageJ) (see lower right in Figure 2). The angle value measured in the image was subsequently corrected for angulation of the imaging slab relative to the main magnetic

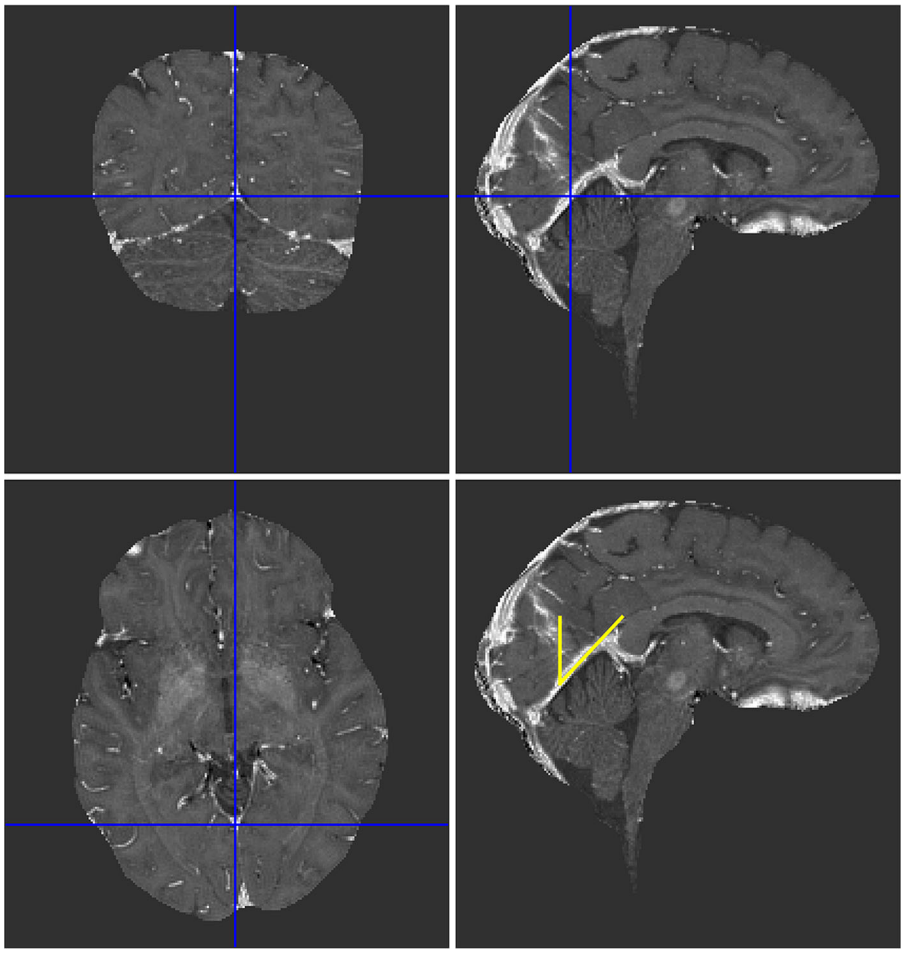

FIGURE 2 Straight sinus vessel analysis in the three principal anatomical planes for determination of the vessel orientation relative to the main magnetic field, required for the oxygen extraction fraction estimation using susceptometry-based oximetry. The vessel angle was estimated in the sagittal plane using an angle measurement tool in the image processing software (ImageJ) (lower right), followed by correction for angulation of the imaging slab to yield the final vessel angle relative to the B_0 direction

JOURNAL OF NEUROIMAGING
THE OFFICIAL JOURNAL OF THE AMERICAN SOCIETY OF NEUROIMAGING

TABLE 2 OEF estimation in SSS

		SSS OEF (%)		
Volunteer number	Absolute vessel angle (°)	QSM	SBO	R2*
1	9	41	37	38
2	0	28	28	41
3	0	29	33	41
4	14	35	36	37
5	0	37	31	35
6	0	39	31	37
7	7	29	30	37
8	13	24	23	33
9	9	40	38	39
10	8	31	29	35
11	0	31	28	33
12	18	24	24	31
13	14	18	18	34
14	0	29	25	27
15	0	28	26	29
16	0	30	27	36
Mean ± SD		31 ± 6	29 ± 5	35 ± 4

Note: Mean oxygen extraction fraction (OEF) and standard deviation (SD) in superior sagittal sinus (SSS) for each subject, estimated by the three different methods, that is, quantitative susceptibility mapping (QSM), susceptometry-based oximetry (SBO), and transverse relaxation rate (R2*). The absolute vessel angle relative to the B_0 direction is also shown.

TABLE 3 OEF estimation in SS

		SS OEF (%)		
Volunteer number	Absolute vessel angle (°)	QSM	SBO	R2*
1	30	49	35	33
2	41	45	71	35
3	25	52	39	33
4	29	45	46	41
5	26	46	52	39
6	34	59	54	39
7	36	37	48	39
8	40	38	69	35
9	34	38	66	41
10	24	40	40	40
11	35	51	55	32
12	19	28	30	31
13	36	33	41	34
14	38	45	59	36
15	25	40	40	37
16	28	41	33	31
Mean ± SD		43 ± 8	49 ± 13	36 ± 3

Note: Mean oxygen extraction fraction (OEF) and standard deviation (SD) in straight sinus (SS) for each subject, estimated by the three different methods, that is, quantitative susceptibility mapping (QSM), susceptometry-based oximetry (SBO), and transverse relaxation rate (R2*). The absolute vessel angle relative to the B_0 direction is also shown.

field to yield the vessel angle relative to the B_0 direction (displayed in Tables 2 and 3).

Before performing a more in-depth analysis of OEF estimates, two challenging postprocessing procedures, believed to have substantial influence on the OEF calculations, were systematically investigated:

1. The dependence of the mean OEF estimates across subjects on the specific fraction of the highest venous values to be included. OEF was, as indicated above, calculated for different threshold levels (0.5, 0.7, 0.75, 0.8, 0.85, 0.90, 0.95) corresponding to inclusion of 50%-5% of the top venous values in the VOI, and compared with the PB OEF estimates (being in general agreement with the manual pilot investigation).
2. The dependence of the QSM-based OEF estimates across subjects on the MEDI regularization parameter λ. The QSM-based OEF values were analyzed for λ values 500, 1000, 2500, 4000, and 7000.

Thereafter, for a venous vessel threshold of 0.8 (illustrated in Figure 3) and $\lambda = 4000$, individual resting-state OEF estimates were obtained for each vessel type (SSS and SS), from phase images using the SBO approach (Equation 4) and by using the QSM maps (Equation 3). OEF assessment based on R2* information was made according to Equation (5). The reasoning behind the specific numerical choices of threshold level and λ value is explained in the DISCUSSION section.

The agreement between OEF values obtained with the different methods was analyzed, as well as the mutual agreement between OEF values obtained from the two different vessel types. Furthermore, possible dependences of the OEF estimates on the vessel angle relative B_0 and the vessel size were investigated for OEF values obtained in the SS. In this context, the SSS was treated as a reference region, due to previously reported validations, established robustness, and several favorable geometric features compared with SS. The vessel size was here represented by the number of remaining VOI venous voxels. The voxel size achieved at 7T was assumed to minimize the probability of PVEs in the larger SSS vessel. Hence, potential manifestations of PVEs related to vessel size were only investigated in the smaller SS vessel.

Statistical analysis

OEF relationships were evaluated by linear regression analysis in combination with extraction of the Pearson correlation coefficient r; the corresponding p-value is the probability of finding the current r value if the correlation had in fact been zero. The agreement between methods was further assessed using Bland-Altman plots.

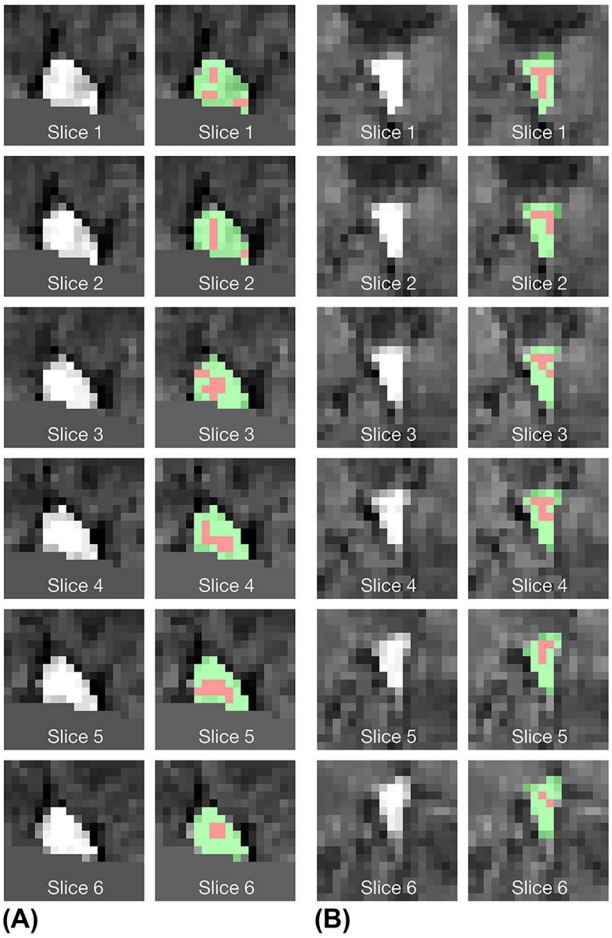

FIGURE 3 Illustration of the application of the venous mask combined with a threshold level of 0.8 in (A) superior sagittal sinus and (B) straight sinus, for each slice of the slab of interest in one volunteer. Defined venous voxels after application of the venous mask are highlighted in green/red, where the red voxels represent the 20% highest values within the venous vessel

RESULTS

Influences of threshold level and regularization parameter λ on OEF estimates

The influence on the mean OEF estimates across subjects when increasing the threshold level of averaged top venous values in the VOI is shown for each method and vessel in Figures 4A (SSS) and 4B (SS). For the different threshold levels (0.5-0.95), the group mean number of included voxels in the analysis was, for SSS, in the range 11 (threshold 0.95) to 100 (threshold 0.5) for QSM, 12-106 for SBO, and 16-151 for R2*, and for SS, the corresponding numbers were 9-83 (QSM), 7-62 (SBO), and 11-99 (R2*). All QSM-based OEF estimates were here obtained with $\lambda = 4000$. The dotted horizontal lines in the graphs, corresponding to the PB OEF estimates (ie, QSM PB, SBO PB, and R2* PB), are included to visualize a comparison with manual ROI selection. The relationship between the QSM-based OEF estimates and the regularization parameter λ is shown for different thresholds of included venous values in SSS (Figure 4C) and in SS (Figure 4D), and QSM images from one representative volunteer, obtained with different λ settings, are shown in Figure 5.

As expected, the OEF estimates increased as the threshold level of included top venous values in the calculations increased; higher threshold implies that only voxels with higher susceptibility values are included in the OEF calculations, which leads to higher estimates of OEF. A clearly larger range of observed QSM-based and SBO-based OEF estimates was seen for SS compared to SSS.

Increased λ yielded higher OEF estimates. This is in accordance with the visual impression of the images in Figure 5, in which the images using low λ values give a somewhat smoother impression, leading to reduced susceptibility values in high-susceptibility structures (eg, in veins such as SS and SSS). The smoothness in the reconstructed QSM map diminished as the regularization parameter increased, and a slight noisiness in some regions was seen at $\lambda = 7000$, but no major artifacts were observed for any λ setting in the investigated interval (500-7000).

Mean values of resting OEF

The OEF results presented below were all obtained by averaging of the 20% highest venous values in the VOI (corresponding to a threshold level of 0.8), and all employed QSM maps were reconstructed with $\lambda = 4000$. OEF estimates for each volunteer and vessel type, estimated by the three different methods, are listed in Table 2 (SSS-based OEF values) and Table 3 (SS-based OEF-values). Slightly low OEF values were seen in SSS. A clear discrepancy in OEF estimates between SSS and SS was noted when using SBO and QSM, both methods showing higher mean values of resting OEF estimates in SS compared to SSS, whereas R2* yielded similar group mean values in both vessels. A larger difference between the methods and a larger SBO variability was noted in SS compared to SSS.

Comparison of OEF estimates obtained using the different methods

Figure 6 shows scatter plots across subjects of OEF estimates in SSS and SS obtained by the different methods: OEF_{SBO} versus OEF_{QSM} (Figure 6A for SSS and Figure 6G for SS), OEF_{R2*} versus OEF_{QSM} (Figure 6B,H), and OEF_{R2*} versus OEF_{SBO} (Figure 6C,I). The corresponding Bland-Altman plots for SSS and SS are shown in Figures 6D-F and 6J-L, respectively. For all displayed scatterplots, each data point represents one individual study subject.

Figure 6A-C indicates that, for SSS, a very good correlation was found between OEF_{SBO} and OEF_{QSM} ($r = .88$, $p < .001$) and a good correlation was observed between OEF_{R2*} and OEF_{SBO} ($r = .65$, $p = .01$), whereas a modest correlation (also with a less convincing intercept) was seen for OEF_{R2*} versus OEF_{QSM} ($r = .44$, $p = .09$). For SS, Figure 6G-I indicates that no meaningful correlations between methods were obtained ($r = .21$, $p = .44$ for OEF_{SBO} vs. OEF_{QSM}, $r = .08$,

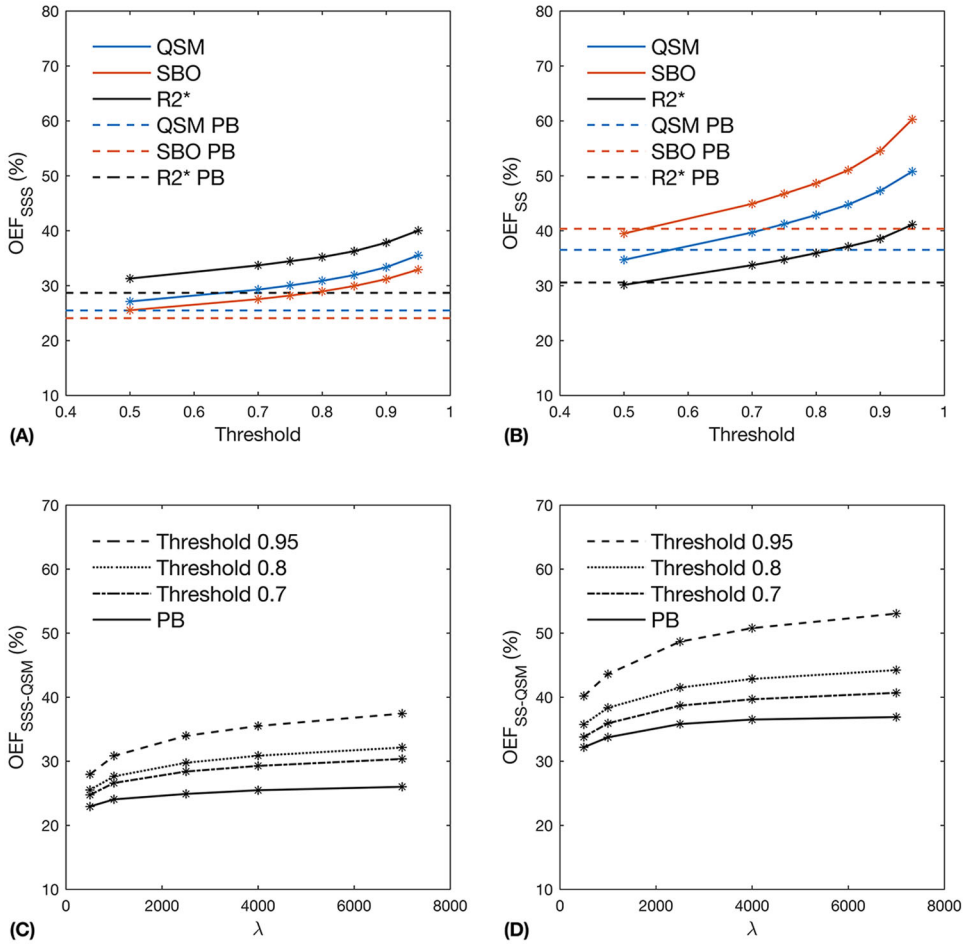

FIGURE 4 Top row: The relationship between group mean oxygen extraction fraction (OEF) and threshold level of included top venous values, for the different methods, that is, quantitative susceptibility mapping (QSM) (regularization parameter $\lambda = 4000$), susceptometry-based oximetry (SBO), and transverse relaxation rate (R2*), in (A) superior sagittal sinus (SSS) and (B) straight sinus (SS). Bottom row: The relationship between QSM-based group mean OEF and λ in (C) SSS and (D) SS for different thresholds of included highest venous values. The threshold value indicates the fraction of venous voxels in the volume of interest that was excluded. PB refers to percentile-based OEF estimates

$p = .76$ for OEF_{R2^*} vs. OEF_{QSM}, and $r = .32$, $p = .22$ for OEF_{R2^*} vs. OEF_{SBO}). The corresponding Bland-Altman plots show only a few outliers, and the systematic bias was somewhat smaller for SSS. A proportional error seemed to be present in the comparisons displayed in Figure 6K,L, and a bias in relation to the R2*-based estimates was substantial in SS.

Dependence of SS OEF estimates on the SS angle relative to B_0

The dependence of the SS OEF values on the SS vessel angle relative to B_0 are shown in Figure 7. In Figure 7A-C, the relation between estimated OEF in SS and the SS angle is plotted for each one of the three different methods, and in Figure 7D-F, the difference of estimated OEFs in SS, between the different methods, is plotted as a function of SS angle.

Figure 7B shows a positive correlation for the SBO-based OEF estimates in relation to the SS angle ($r = .79$, $p < .001$), and, as a consequence, a trend toward an OEF difference dependence on SS angle can be noticed in the two scatter plots that include SBO-based estimates (Figure 7D,F) ($r = .67$, $p = .01$ for OEF_{SBO}-OEF_{QSM} and $r = .82$, $p < .001$ for OEF_{SBO}-OEF_{R2^*}). Also, in Figure 7D-F, the two data points that correspond to the smallest angles generally show differences close to zero.

Comparison of OEF estimates between the two vessels

Figure 8 shows the investigated mutual agreement of OEF in SSS and SS using the three different methods: QSM (Figure 8A), SBO (Figure 8B), and R2* (Figure 8C). A significant moderate degree of correlation between OEF estimates obtained in SSS and SS can be noted only when QSM was used ($r = .61$, $p = .01$).

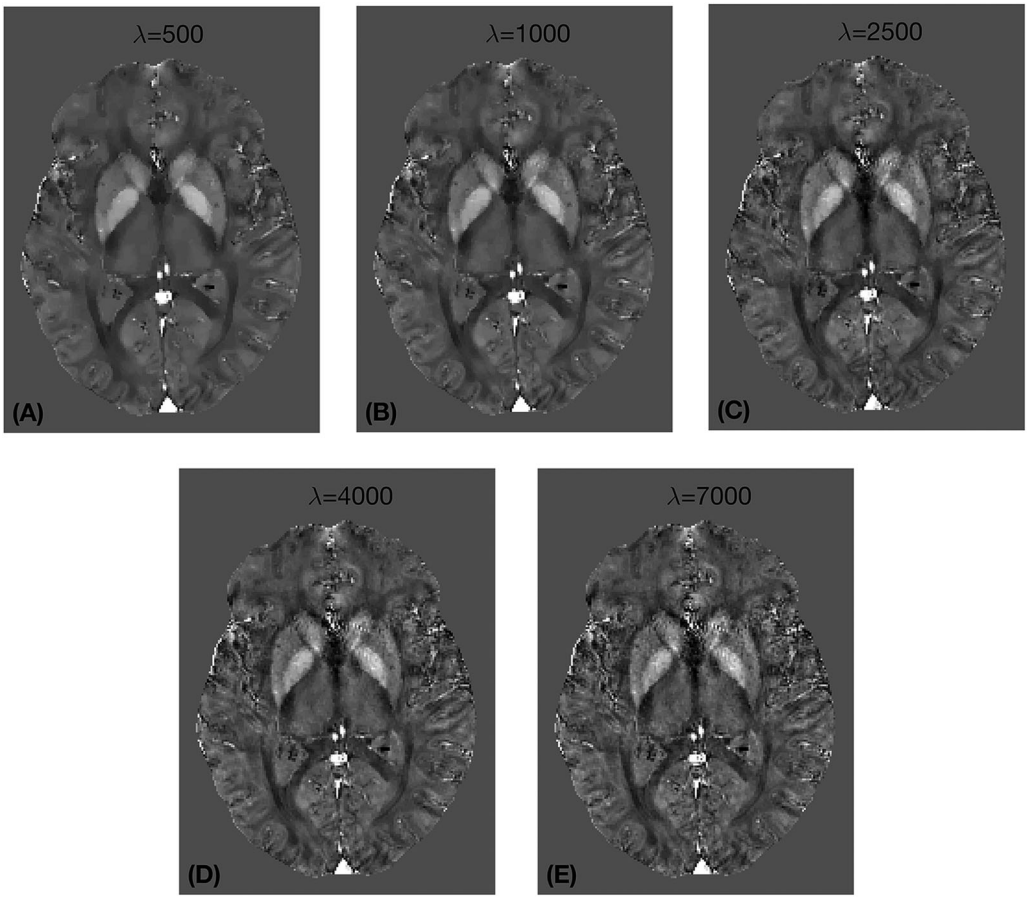

FIGURE 5 Quantitative susceptibility maps from one representative volunteer, obtained with different settings of the regularization parameter λ: (A) 500, (B) 1000, (C) 2500, (D) 4000, and (E) 7000

OEF dependence on SS size and SS angle relative to B_0

The difference between measured OEF in the two vessel types, when applying the different methods, is plotted as a function of observed SS angle relative to B_0 (Figure 9A-C) as well as SS size (Figure 9D-F). Figure 9B indicates an SS angle dependence when using SBO ($r = .80$, $p < .001$), that is, the difference between obtained OEF estimates in SSS and SS increases as the SS angle increases. Figure 9D-F shows that no vessel size dependence can be established for any of the methods used ($r = .01$, $p = .97$ for QSM, $r = .18$, $p = .49$ for SBO, and $r = .03$, $p = .93$ for R2*).

DISCUSSION

In this study, global resting OEF values in healthy subjects were investigated, using three different OEF calculation methods (QSM, SBO, and R2*) in two major draining veins (SS and SSS) representing different geometric conditions. The employed postprocessing and analysis procedures included several steps that may influence the results, and some of these steps were systematically investigated.

Methodological considerations

First, accurate identification of voxels assumed to represent purely venous information is a source of concern, and the procedure, with the aim to minimize PVEs and other confounding factors, has varied considerably between previously published studies.[20,27,34,36,41,55,56] In the present study, the selection of appropriate venous values for obtaining the QSM-, phase-, and R2*-based OEF estimates was performed in a semiautomated manner to reduce user dependence. Because the result of this process has a direct impact on the OEF estimates, a comparative investigation of some reasonable options was initially performed. The PB approach for defining the PVE-free venous values provided low OEF estimates compared to the threshold-based approach, indicating a substantial residual risk of PVE influence in manual selection of venous voxels. Regarding thresholding, a relatively high threshold level, including only a small fraction of the highest venous values, is preferred to minimize PVEs. On the other hand, too small a number of remaining values is statistically unfavorable and will decrease the precision, and high thresholds may also result in excessive influence from voxel values corrupted by flow artifacts. Figure 4A,B reveals the large dependence of OEF estimates upon the fraction of included venous values.

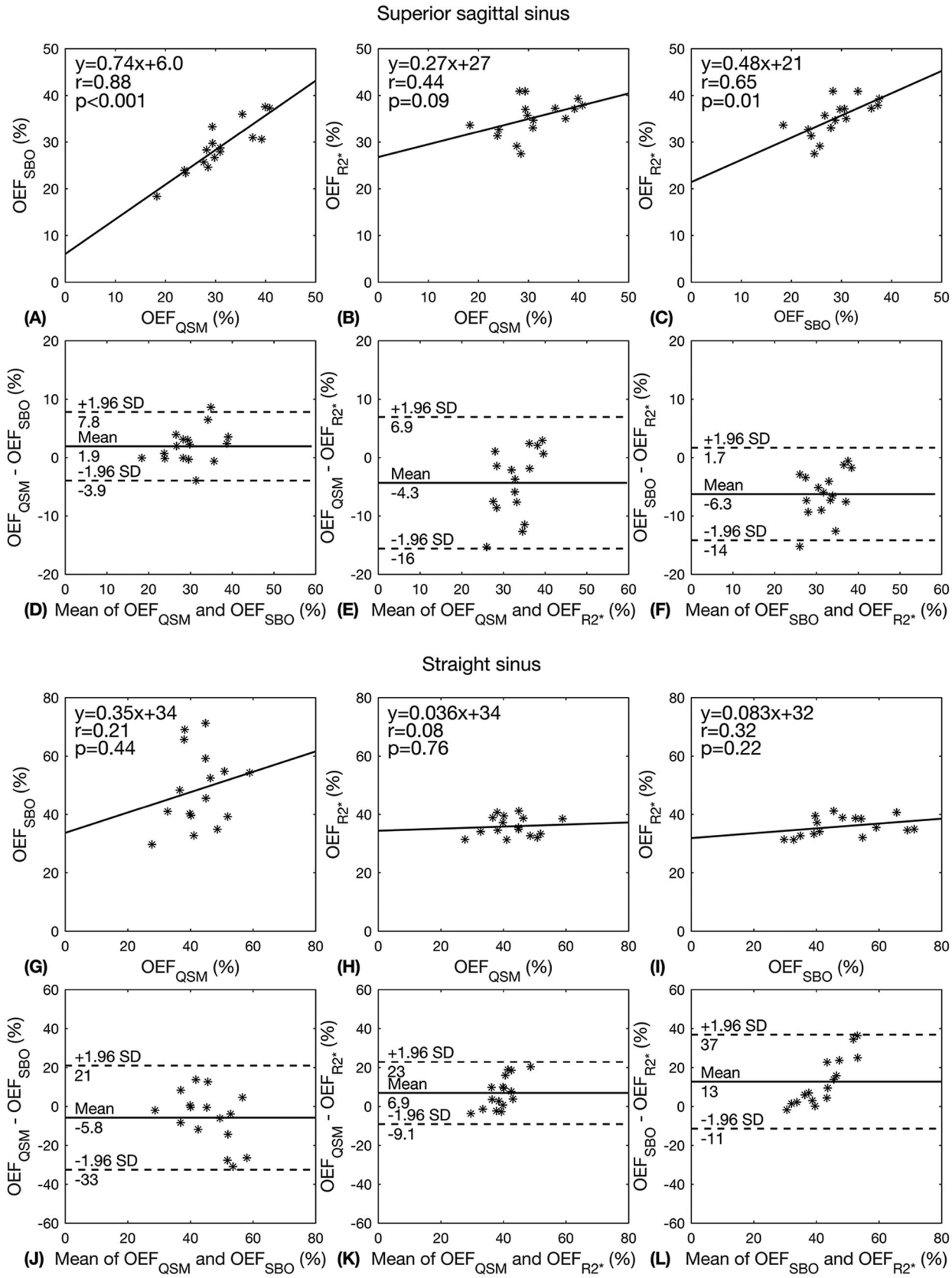

FIGURE 6 The top panel (A-F) corresponds to the superior sagittal sinus and the bottom panel (G-L) corresponds to the straight sinus. (A-C and G-I) Correlations between estimated oxygen extraction fraction (OEF) measured by the different methods, that is, quantitative susceptibility mapping (QSM), susceptometry-based oximetry (SBO), and transverse relaxation rate (R2*): (A, G) OEF_{SBO} versus OEF_{QSM}, (B, H) OEF_{R2^*} versus OEF_{QSM}, and (C, I) OEF_{R2^*} versus OEF_{SBO}. (D-F and J-L) Bland-Altman plots of consistency between OEF estimates obtained by the different methods: (D, J) OEF_{SBO} versus OEF_{QSM}, (E, K) OEF_{R2^*} versus OEF_{QSM}, and (F, L) OEF_{R2^*} versus OEF_{SBO}. The solid line represents the mean OEF difference between the compared methods and the dashed lines denote mean ± 1.96 standard deviation (SD)

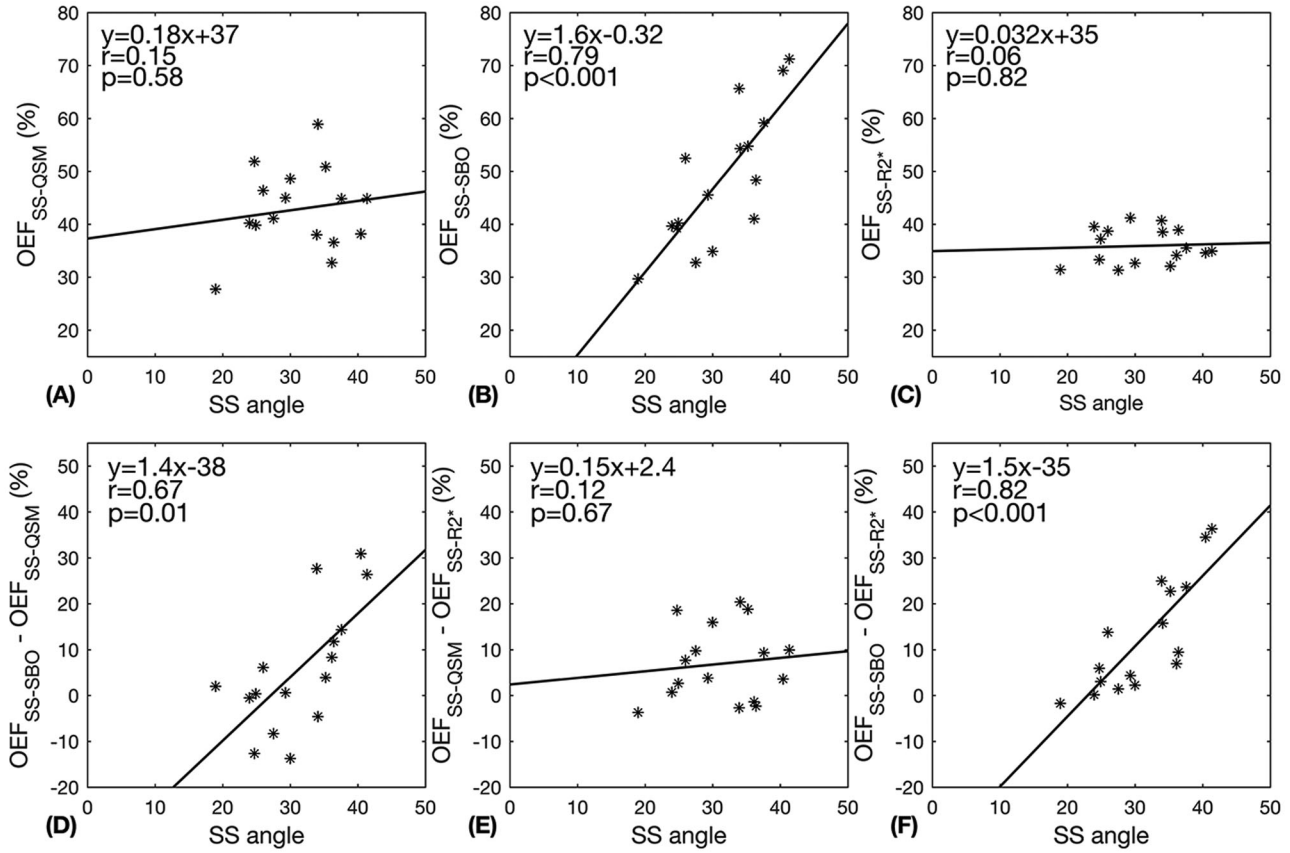

FIGURE 7 Top row: Estimated oxygen extraction fraction (OEF) in straight sinus (SS) versus the SS angle for the three different methods, that is, (A) quantitative susceptibility mapping (QSM), (B) susceptometry-based oximetry (SBO), and (C) transverse relaxation rate (R2*). Bottom row: Difference in SS OEF estimates between methods versus the SS angle: (D) ($OEF_{SBO}-OEF_{QSM}$) versus SS angle, (E) ($OEF_{QSM} - OEF_{R2*}$) versus SS angle, and (F) ($OEF_{SBO} - OEF_{R2*}$) versus SS angle

Interestingly, the SS showed a larger observed range of SBO- and QSM-based OEF estimates as a function of threshold than the SSS (cf. Figure 4A,B). This larger sensitivity to the choice of threshold level in SS can possibly be related to a generally smaller number of included voxels in the SS compared to the SSS, leading to a generally larger statistical uncertainty in SS estimates. Furthermore, for a large vessel, PVEs are less likely to manifest themselves even if the threshold is changed to lower levels. Thus, it is generally reasonable that a larger vessel, such as the SSS, would show a lower PVE-related sensitivity to changes in threshold level and provide more stable results, compared

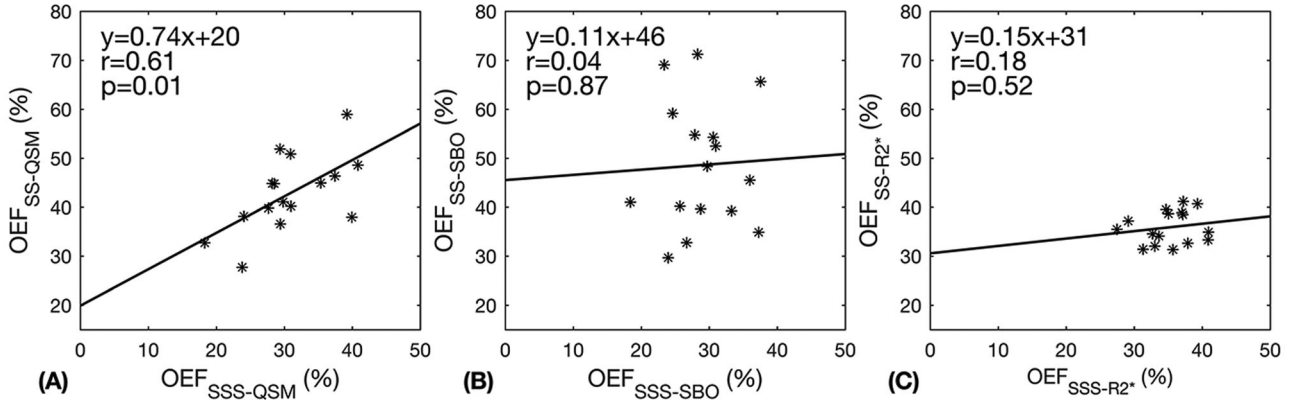

FIGURE 8 Oxygen extraction fraction (OEF) in straight sinus (SS) versus OEF in superior sagittal sinus (SSS) when using the different methods, that is, (A) quantitative susceptibility mapping (QSM), (B) susceptometry-based oximetry (SBO), and (C) transverse relaxation rate (R2*)

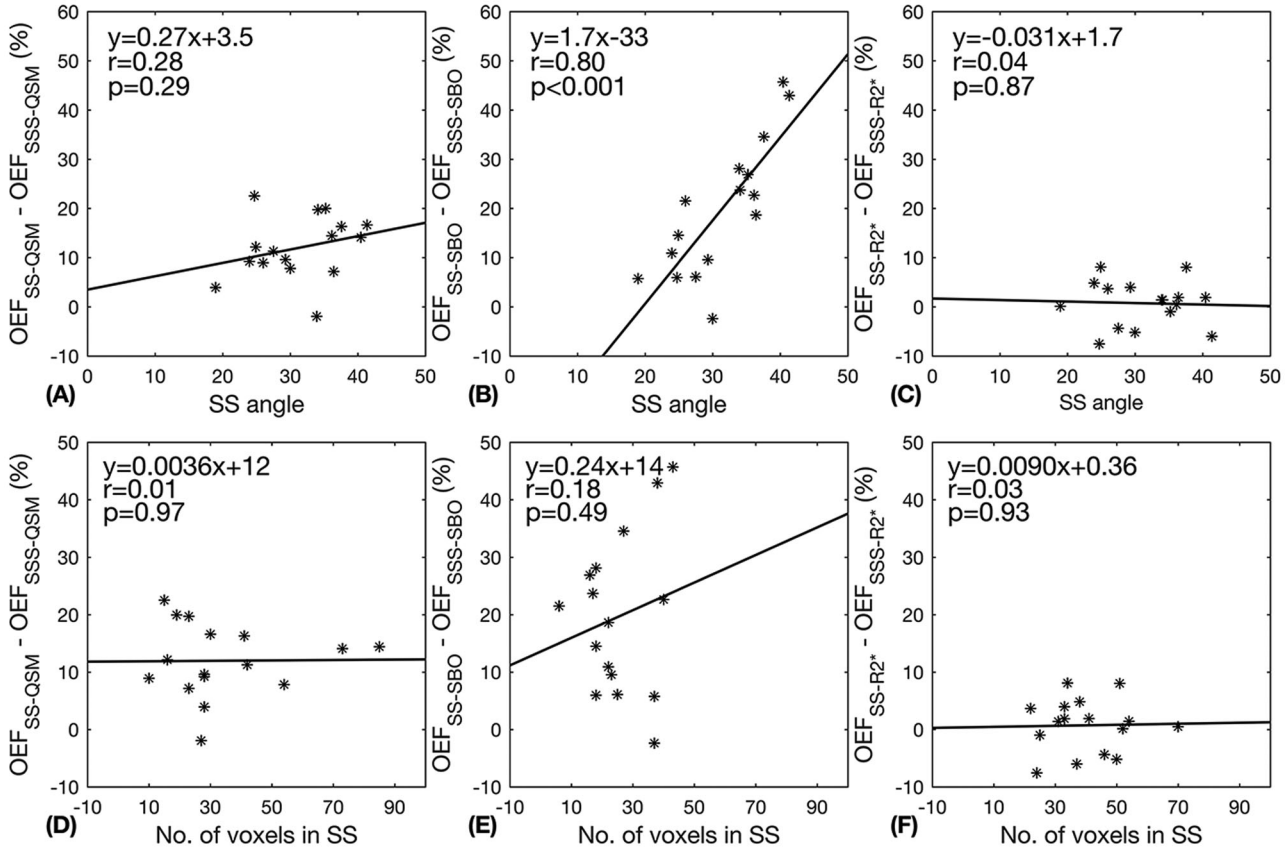

FIGURE 9 Top row: The difference between oxygen extraction fraction (OEF) estimates in the two vessel types (superior sagittal sinus [SSS] and straight sinus [SS]) as a function of the SS angle relative to B_0, when using the different methods, that is, quantitative susceptibility mapping (QSM), susceptometry-based oximetry (SBO), and transverse relaxation rate (R2*): (A) ($OEF_{SS-QSM} - OEF_{SSS-QSM}$) versus SS angle, (B) ($OEF_{SS-SBO} - OEF_{SSS-SBO}$) versus SS angle, and (C) ($OEF_{SS-R2*} - OEF_{SSS-R2*}$) versus SS angle (C). Bottom row: (D-F) Corresponding analysis of OEF difference as a function of SS size (here represented by the number [no.] of voxels in SS)

to SS. To improve future studies, a digital brain phantom analysis, with known susceptibilities in relevant compartments, can be considered, to serve as a guideline to minimize the probability of suboptimal choice of venous values.

Second, in QSM reconstruction using MEDI, one important challenge is to determine the optimal regularization weighting parameter λ for OEF quantification. Increased OEF estimates associated with increased λ were, as expected, observed (Figure 4C,D). Reasonable QSM images without significant artifacts could still be reconstructed with the highest λ (ie, 7000), although a modest increase in noisiness was noticed for the highest value. Increased λ in MEDI yields an increased susceptibility difference between venous vessels and surrounding tissue, and in previous investigations this has been associated with improved quantitative accuracy. Specifically, for quantification, Liu et al.[42] noted that low λ values need to be avoided (in spite of providing smooth QSM maps), whereas a high degree of accuracy (assessed from the slope of the linear regression between the reconstructed susceptibilities and the true values) could be achieved over a rather wide range of higher λ values.[42]

In summary, Figure 4 aims at providing an indication of the bias that may be introduced by using different settings; Figure 4A,B clarifies the importance of the choice of voxels representing PVE-free venous blood and Figure 4C,D displays the variability introduced by the λ setting, for the resulting OEF estimates. Taking the above issues into account, the subsequent discussion is based on OEF results obtained by averaging of the top 20% of the venous values (avoiding the steeper increase seen at higher thresholds, possibly related to increased influence of flow artifacts) and by using $\lambda = 4000$ (fairly steady level at threshold 0.8 and no pronounced noisiness). When interpreting the discussion below and the comparisons with other studies, one needs to be aware of the variability that can be introduced by varying these settings.

SSS shows several favorable geometric conditions compared with SS, that is, larger diameter, smaller and more well-defined angle relative to B_0, and increased vessel length-to-diameter ratio, and this should contribute to more reliable and accurate OEF estimates in the SSS. However, the initial investigations, especially for SBO and QSM, indicated, in general, somewhat low OEF estimates compared to previously reported global OEF measurements, as further discussed below.

Uncertainties in quantification may also be introduced by the location of the vessel close to the brain surface, due to the established QSM reconstruction difficulties near tissue-air boundaries.[38,39] In MEDI, it is also necessary to define an ROI that includes the susceptibility sources

generating the local field, that is, a mask of the brain needs to be defined. Using the MEDI toolbox, the brain mask was, in this study, automatically defined based on magnitude information and individually adapted to each subject. Because uncertainties in phase values translate into errors in the reconstructed susceptibility map, slices of the lower part of the brain, corresponding to regions outside the volume of interest, were manually excluded from the mask in all subsequent processing. However, because SSS is located in the very outer part of the brain mask, a more thorough investigation of mask influence on the quantitative values and appearance of SSS could be considered in future studies.

As indicated above, another potential source of uncertainty in the phase values may be related to flow artifacts and flow compensation. In this study, flow compensation to correct for motion-induced dephasing and accumulated phase shifts of moving spins was only performed for even echoes in the readout direction. Thus, residual flow artifacts may contribute to OEF uncertainties, especially in large vessels.[35] However, the effect in this study is most likely relatively small; a brief pilot investigation in three randomly chosen subjects yielded only minor quantitative variations in the local field and susceptibility maps when using images acquired either with odd or even echoes.

Mean values of resting OEF

The mean values of resting OEF in SSS varied from 29% to 35% between the methods, and the mean values can, as mentioned above, be considered a bit low compared to previously reported global OEF estimates, for example, 39% ± 6%[57] and 43% ± 6%[58] obtained by ^{15}O PET. Somewhat low SBO-based OEF estimates in SSS, ranging between 31% and 35%, have previously been reported.[20,21,40,59,60]

It should, in this context, be emphasized that the susceptibility-based quantification of venous blood oxygenation depends on $\Delta\chi_{do}$, and the chosen numerical value of this constant strongly influences the OEF estimates. For example, older literature values include $\Delta\chi_{do} = 0.18 \cdot 4\pi$ ppm[16] and $\Delta\chi_{do} = 0.2 \cdot 4\pi$ ppm.[8,61] In the present study, $\Delta\chi_{do} = 0.27 \cdot 4\pi$ ppm was employed, as recommended by Spees et al.[43] and Jain et al.[44] There has been some doubt about the most appropriate choice, and both $0.27 \cdot 4\pi$ and $0.18 \cdot 4\pi$ are stated in a standard MRI textbook.[62] The lowest value has been used in several studies,[17,18,20,37] whereas the highest value has become more common in recent years.[21,34,40,41,44,56] However, a very recent and compelling investigation, focusing on in vivo conditions, arrived at $\Delta\chi_{do} = 0.193 \cdot 4\pi$ ppm,[63] and if this value were to be applied to the data of this study, the susceptibility-based SSS OEF estimates would be 43% ± 9% (QSM) and 40% ± 7% (SBO), in excellent agreement with previous PET-based OEF results.

A dependence on vessel type (ie, an OEF difference between vessels at different spatial locations) was noted for SBO and QSM, but not for R2*. The former two methods produced notably different OEF estimates in SS compared to SSS, and this observed variability, also documented by Fan et al.,[34] does, most likely, not reflect a true physiological difference because the oxygenation level across the healthy brain is fairly uniform, according to previous PET studies, and only reported to be slightly lower in sensorimotor cortex.[64] Hence, in this study, the differences between SS and SSS are attributed to various methodological issues, and the assumption that SSS estimates are likely to be more accurate gives an opportunity to systematically investigate probable sources of uncertainty, as further discussed below.

The difference between the methods was higher in SS compared to SSS and the variability of the OEF estimates among individuals was markedly higher in SS for SBO, possibly due to varying SS angles relative B_0 for different individuals. Vessel-type dependence and interindividual variability were lowest for R2*, which may well reflect a strength of this method. However, this observation does not necessarily imply a high degree of trueness, as further reflected upon below. A certain degree of natural biological variation among subjects is expected, due to, for example, age and minor fluctuations related to individual state of stress and cerebral activity during scanning, and the range of normal OEF values is approximately 29%-45%.[65] Furthermore, Hattori et al.[57] reported the full range (min-max) of observed OEF values to be 30%-51%. It would thus not be unexpected to see a similar range in the current results.

Comparison of OEF estimates obtained using the different methods

Reasonable degrees of correlation between the methods were only seen in SSS. In similar situations, SBO has previously been stated as one of the most accurate methods for global OEF quantification.[21] Consequently, as a very good correlation was found between SBO and QSM (r = .88), QSM can be considered to be successfully validated in a vessel being almost parallel with the main magnetic field. Regarding SS, no meaningful correlations could be observed, and the corresponding Bland-Altman plots indicated a proportional error in the figures related to comparison with R2* (Figure 6K,L). One possible explanation might be related to the reduced variability in OEF estimates for the R2*-based values compared with the other two methods.

Dependence of SS OEF estimates on the SS angle relative to B_0

The applied infinite cylinder approximation is only valid to a certain degree, depending on, for example, nonperfect circular cross section, finite length, vessel curvature, and imprecise measurement of vessel tilt angle, and this must be considered when interpreting the SBO results. The model is better suited for small vessel angles; for a given OEF estimate, larger vessel angles will, according to Equation (4), be associated with smaller phase shifts between the intra- and extravascular compartments, hence reducing the precision of the OEF quantification. Furthermore, the influence of the precision in measured angle also increases as the vessel tilt increases, and a 10% uncertainty

in vessel tilt angle results in nearly 40% error in estimations of venous oxygen saturation for vessel angles near the magic angle.[26] The accuracy and precision of the infinite-cylinder model required in SBO have been investigated in previous studies,[18,25,26] and even if the influence of the aforementioned confounding factors was small in most cases, most of the analysis only included vessel tilt angles <30°. Simulations, performed by Fernández-Seara et al.,[18] including a wide range of oxygenation levels, clearly indicated a substantially increased error in the oxygen saturation measurements as the vessel tilt relative to B_0 increased and approached the magic angle.[18]

One possible explanation to the poor OEF agreement among methods in SS might thus be related to the results shown in Figure 7. Here, the robustness of SBO appears to be lost. Figure 7B shows a strong dependence of SBO-based OEF estimates on SS vessel angle. Consequently, the OEF difference between the methods increased with increasing angle in the two scatter plots that include SBO-based OEF estimates (Figure 7D,F). However, no such angle dependence is displayed by QSM and R2*, indicating higher robustness across different vessel orientations.

Comparison of OEF estimates between the two vessels and OEF dependence on SS angle

When OEF estimates are compared between the two vessels, a correlation was only noted for QSM results (Figure 8A), indicating that QSM is, as expected, more robust to differences in object geometry, shape, and orientation. Sources of the exhibited variation between the two vessels and the poor agreement for SBO most likely include a residual angle-dependent bias in SBO (Figure 9B).

Even if the concept of QSM is supposed to resolve the issues of nonlocal and orientation-dependent phase, phantom simulations in previous work have shown inaccurate susceptibility values at large angles relative to the main magnetic field.[34,66] For example, a bias related to vessel angle for QSM has been noticed, showing a maximum around 45 degrees.[34] No such bias could, however, be observed in this study, but it is possible that relatively small vessel angles and the interindividual variability of OEF within the cohort tended to conceal any such bias.

The nonexisting correlation for R2* was somewhat unexpected as the group mean values obtained in the two vessels were similar. The mean values of T2* in the two investigated vessels were 5.6 ms (SSS) and 5.5 ms (SS). Hence, the applied TEs seem reasonable with respect to estimations of venous T2*. However, it can be worth mentioning that if the true interval of OEF estimates is, hypothetically, better represented by a somewhat more restricted range of values, as indicated by the R2*-based measurements, the correlation will automatically be reduced, which may mislead and complicate a correlation comparison between the methods.

No angle dependence was revealed for R2*, which seems reasonable for the conditions inside a vessel and is a clear general advantage with the R2* method. However, other issues are important for the R2* method. R2* maps are susceptible to several parameters, other than dHb, that will cause spin dephasing and consequently affect the accuracy of R2*-based OEF estimates. R2* maps are dependent on parameters such as field strength, echo time, voxel size, and object orientation. Furthermore, R2* is sensitive to macroscopic B_0 inhomogeneities (shim, air/tissue interface), the R2 component, water diffusion, and characteristics of the blood vessel network.[67,68] This contributes to lowering the potential of quantitatively mapping dHb in vivo by use of R2*. Another potential inaccuracy of the R2*-based OEF values is related to the assumed relation between dHb content and R2* at 7T. Obviously, uncertainties in the mathematical representation (Equation 5), related to limited goodness-of-fit and dissimilar experimental conditions or blood properties (eg, hematocrit level), will possibly translate to errors in obtained R2*-based OEF estimates.

OEF dependence on SS size

As mentioned above, PVEs are also a possible reason for observed variations of oxygen saturation in vessels of different diameter.[34] Smaller vessels are to a greater extent associated with PVEs, yielding a decreased apparent susceptibility difference between the vessel and the surroundings. The manifestation of PVEs in phase and QSM data is, however, not entirely straightforward. For example, if PVEs are present, the phase of a cylinder shows a complex behavior that depends on the radius of the cylinder in relation to the voxel size.[33,69] The investigation of the dependence of OEF on SS size in this study was not able to confirm any dependence on the included number of voxels (Figure 9D-F). It is possible that the small voxel size in combination with the chosen threshold level did, in fact, minimize PVE effects in all larger draining vessels, including the investigated SS vessel.

Other sources of errors

Finally, there are additional sources of uncertainty in the measurements and the analysis procedure. To perform QSM, reliable phase data are essential, and it should be noted that the use of bipolar gradients can cause artifacts in the slice and readout directions in the phase images, manifested as a linear phase error.[70] However, in the present study, no obvious linear artifacts were visually observed in the phase images after the removal of background field contributions using the PDF method. Another limitation is that some parameters in the calculations were set to a constant value regardless of existing individual variations. For example, arterial blood oxygenation was assumed to be 100%, but this value is known to vary slightly, typically between 95% and 100%, also in healthy subjects.[56] In terms of magnetic susceptibility, tissue with a susceptibility dominated by that of water was assumed to represent arterial blood in this study, and one might thus consider also to include the diamagnetic susceptibility shift between oxygenated erythrocytes and water (ie, $\Delta\chi_{oxy-water} = -0.03$ ppm)[16] in Equation (3), but this correction is often omitted as it is regarded to be insignificant in comparison with the significantly larger paramagnetic susceptibility shift driven by the dHb (ie, $\Delta\chi_{do} = 0.27 \cdot 4\pi$

in this study). Furthermore, the hematocrit value was assumed to be Hct = 0.4 for all subjects, but there is a significant variability between individuals as well as a gender dependence. Typical values range between 0.37 and 0.47 for females and between 0.40 and 0.54 for males.[71] Having this parameter carefully measured for each subject in future studies would increase the accuracy of the OEF estimates.

Conclusions and future considerations

In conclusion, the QSM approach appeared to enable oxygenation assessment over a large range of vessel angles relative to B_0. The QSM method showed reasonable OEF correlation between vessels of different geometries, very good correlation with SBO-based OEF estimates in SSS (ie, under conditions where SBO-based OEF measurements are previously well established), and limited angular dependence. For both QSM and SBO, the OEF mean values differed between SS and SSS, and SBO showed a pronounced SS vessel angle dependence. R2*-based estimates showed no vessel angle dependence and the lowest OEF interindividual variability in combination with convincing OEF mean values. On the other hand, the observed OEF range appeared slightly low compared with the expected natural biological variability. Neither R2* nor SBO showed any meaningful correlations when mutually comparing OEF estimates from the two vessels. Overall, this study suggests that QSM holds promise to become an accurate and robust method for OEF estimation across different vessel orientations, but the estimation of absolute levels (for both SBO and QSM) requires that a consensus is reached regarding the correct value of $\Delta\chi_{do}$. Extension of the QSM approach to a range of vessel orientations and sizes has been nicely demonstrated, for example, by Fan et al.[34] at 3T. The introduction of ultrahigh-field MRI units implies higher sensitivity to dHb and improved spatial resolution, and may thus allow for vessels of smaller diameter to be captured, but the increased risk of image distortions close to tissue-air interfaces may need to be counteracted by the use of higher bandwidth pulse sequences. Finally, an important potential future clinical application relates to how the severe acute respiratory syndrome corona virus 2 (SARS CoV-2) can affect the microcirculation; inflammation and damage to blood capillaries may cause acute and long-term COVID-19 symptoms by influencing blood and brain oxygenation.[72]

ACKNOWLEDGMENT AND DISCLOSURE

Swedish Research Lund University Bioimaging Center (LBIC) is acknowledged for experimental resources (equipment grant VR RFI 829-2010-5928). The funding sources had no further involvement in this work.

The authors declare no conflict of interest.

ORCID

Ronnie Wirestam https://orcid.org/0000-0003-2628-0760

REFERENCES

1. Christen T, Bolar DS, Zaharchuk G. Imaging brain oxygenation with MRI using blood oxygenation approaches: methods, validation, and clinical applications. AJNR Am J Neuroradiol 2013;34:1113-23.
2. Derdeyn CP, Videen TO, Yundt KD, et al. Variability of cerebral blood volume and oxygen extraction: stages of cerebral haemodynamic impairment revisited. Brain 2002;125:595-607.
3. Heiss WD. Ischemic penumbra: evidence from functional imaging in man. J Cereb Blood Flow Metab 2000;20:1276-93.
4. Schell RM, Cole DJ. Cerebral monitoring: jugular venous oximetry. Anesth Analg 2000;90:559-66.
5. Sakudo A. Near-infrared spectroscopy for medical applications: current status and future perspectives. Clin Chim Acta 2016;455:181-8.
6. Baron JC, Jones T. Oxygen metabolism, oxygen extraction and positron emission tomography: historical perspective and impact on basic and clinical neuroscience. Neuroimage 2012;61:492-504.
7. Pauling L, Coryell CD. The magnetic properties and structure of hemoglobin, oxyhemoglobin and carbonmonoxyhemoglobin. Proc Natl Acad Sci USA 1936;22:210-6.
8. Thulborn KR, Waterton JC, Matthews PM, et al. Oxygenation dependence of the transverse relaxation time of water protons in whole blood at high field. Biochim Biophys Acta 1982;714:265-70.
9. Bandettini PA, Wong EC, Jesmanowicz A, et al. Spin-echo and gradient-echo EPI of human brain activation using BOLD contrast: a comparative study at 1.5 T. NMR Biomed 1994;7:12-20.
10. Wright GA, Hu BS, Macovski A. Estimating oxygen saturation of blood in vivo with MR imaging at 1.5 T. J Magn Reson Imaging 1991;1:275-83.
11. Blockley NP, Jiang L, Gardener AG, et al. Field strength dependence of R1 and R2* relaxivities of human whole blood to ProHance, Vasovist, and deoxyhemoglobin. Magn Reson Med 2008;60:1313-20.
12. Blockley NP, Griffeth VE, Simon AB, et al. A review of calibrated blood oxygenation level-dependent (BOLD) methods for the measurement of task-induced changes in brain oxygen metabolism. NMR Biomed 2013;26:987-1003.
13. He X, Yablonskiy DA. Quantitative BOLD: mapping of human cerebral deoxygenated blood volume and oxygen extraction fraction: default state. Magn Reson Med 2007;57:115-26.
14. Lu H, Ge Y. Quantitative evaluation of oxygenation in venous vessels using T2-Relaxation-Under-Spin-Tagging MRI. Magn Reson Med 2008;60:357-63.
15. Cerdonio M, Morante S, Vitale S. Magnetic susceptibility of hemoglobins. Methods Enzymol 1981;76:354-71.
16. Weisskoff RM, Kiihne S. MRI susceptometry: image-based measurement of absolute susceptibility of MR contrast agents and human blood. Magn Reson Med 1992;24:375-83.
17. Haacke EM, Lai S, Reichenbach JR, et al. In vivo measurement of blood oxygen saturation using magnetic resonance imaging: a direct validation of the blood oxygen level-dependent concept in functional brain imaging. Hum Brain Mapp 1997;5:341-6.
18. Fernandez-Seara MA, Techawiboonwong A, Detre JA, et al. MR susceptometry for measuring global brain oxygen extraction. Magn Reson Med 2006;55:967-73.
19. Jain V, Langham MC, Wehrli FW. MRI estimation of global brain oxygen consumption rate. J Cereb Blood Flow Metab 2010;30:1598-607.
20. Kämpe R, Lind E, Ståhlberg F, et al. Quantification of normal cerebral oxygen extraction and oxygen metabolism by phase-based MRI susceptometry: evaluation of repeatability using two different imaging protocols. Clin Physiol Funct Imaging 2017;37:211-20.
21. Rodgers ZB, Englund EK, Langham MC, et al. Rapid T2- and susceptometry-based CMRO2 quantification with interleaved TRUST (iTRUST). Neuroimage 2015;106:441-50.

22. Xu F, Ge Y, Lu H. Noninvasive quantification of whole-brain cerebral metabolic rate of oxygen ($CMRO_2$) by MRI. Magn Reson Med 2009;62:141-8.
23. Jain V, Magland J, Langham M, et al. High temporal resolution in vivo blood oximetry via projection-based T2 measurement. Magn Reson Med 2013;70:785-90.
24. Langham MC, Magland JF, Floyd TF, et al. Retrospective correction for induced magnetic field inhomogeneity in measurements of large-vessel hemoglobin oxygen saturation by MR susceptometry. Magn Reson Med 2009;61:626-33.
25. Langham MC, Magland JF, Epstein CL, et al. Accuracy and precision of MR blood oximetry based on the long paramagnetic cylinder approximation of large vessels. Magn Reson Med 2009;62:333-40.
26. Li C, Langham MC, Epstein CL, et al. Accuracy of the cylinder approximation for susceptometric measurement of intravascular oxygen saturation. Magn Reson Med 2012;67:808-13.
27. Fan AP, Benner T, Bolar DS, et al. Phase-based regional oxygen metabolism (PROM) using MRI. Magn Reson Med 2012;67:669-78.
28. Salomir R, de Senneville BD, Moonen CTW. A fast calculation method for magnetic field inhomogeneity due to an arbitrary distribution of bulk susceptibility. Concepts Magn Reson Part B: Magn Reson Eng 2003;19B:26-34.
29. Marques JP, Bowtell R. Application of a Fourier-based method for rapid calculation of field inhomogeneity due to spatial variation of magnetic susceptibility. Concepts Magn Reson Part B: Magn Reson Eng 2005;25B:65-78.
30. Shmueli K, de Zwart JA, van Gelderen P, et al. Magnetic susceptibility mapping of brain tissue in vivo using MRI phase data. Magn Reson Med 2009;62:1510-22.
31. de Rochefort L, Liu T, Kressler B, et al. Quantitative susceptibility map reconstruction from MR phase data using Bayesian regularization: validation and application to brain imaging. Magn Reson Med 2010;63:194-206.
32. Deistung A, Schweser F, Reichenbach JR. Overview of quantitative susceptibility mapping. NMR Biomed 2017;30:e3569.
33. Haacke EM, Tang J, Neelavalli J, et al. Susceptibility mapping as a means to visualize veins and quantify oxygen saturation. J Magn Reson Imaging 2010;32:663-76.
34. Fan AP, Bilgic B, Gagnon L, et al. Quantitative oxygenation venography from MRI phase. Magn Reson Med 2014;72:149-59.
35. Xu B, Liu T, Spincemaille P, et al. Flow compensated quantitative susceptibility mapping for venous oxygenation imaging. Magn Reson Med 2014;72:438-45.
36. Kudo K, Liu T, Murakami T, et al. Oxygen extraction fraction measurement using quantitative susceptibility mapping: comparison with positron emission tomography. J Cereb Blood Flow Metab 2016;36:1424-33.
37. Uwano I, Kudo K, Sato R, et al. Noninvasive assessment of oxygen extraction fraction in chronic ischemia using quantitative susceptibility mapping at 7 tesla. Stroke 2017;48:2136-41.
38. Vinayagamani S, Sheelakumari R, Sabarish S, et al. Quantitative susceptibility mapping: technical considerations and clinical applications in neuroimaging. J Magn Reson Imaging 2021;53:23-37.
39. Wang Y, Liu T. Quantitative susceptibility mapping (QSM): decoding MRI data for a tissue magnetic biomarker. Magn Reson Med 2015;73:82-101.
40. Barhoum S, Rodgers ZB, Langham M, et al. Comparison of MRI methods for measuring whole-brain venous oxygen saturation. Magn Reson Med 2015;73:2122-8.
41. Fan AP, Schafer A, Huber L, et al. Baseline oxygenation in the brain: correlation between respiratory-calibration and susceptibility methods. Neuroimage 2016;125:920-31.
42. Liu J, Liu T, de Rochefort L, et al. Morphology enabled dipole inversion for quantitative susceptibility mapping using structural consistency between the magnitude image and the susceptibility map. Neuroimage 2012;59:2560-8.
43. Spees WM, Yablonskiy DA, Oswood MC, et al. Water proton MR properties of human blood at 1.5 Tesla: magnetic susceptibility, T1, T2, T2*, and non-Lorentzian signal behavior. Magn Reson Med 2001;45:533-42.
44. Jain V, Abdulmalik O, Propert KJ, et al. Investigating the magnetic susceptibility properties of fresh human blood for noninvasive oxygen saturation quantification. Magn Reson Med 2012;68:863-7.
45. Guyton AC, Hall JE. Red blood cells, anemia, and polycythemia. In: Guyton AC, Hall JE, editors. Textbook of medical physiology. Philadelphia, PA: Saunders; 2000:382-91.
46. Olsson H, Andersen M, Lätt J, et al. Reducing bias in dual flip angle T1-mapping in human brain at 7T. Magn Reson Med 2020;84:1347-58.
47. Liu T, Liu J, de Rochefort L, et al. Morphology enabled dipole inversion (MEDI) from a single-angle acquisition: comparison with COSMOS in human brain imaging. Magn Reson Med 2011;66:777-83.
48. Liu T, Wisnieff C, Lou M, et al. Nonlinear formulation of the magnetic field to source relationship for robust quantitative susceptibility mapping. Magn Reson Med 2013;69:467-76.
49. de Rochefort L, Brown R, Prince MR, et al. Quantitative MR susceptibility mapping using piece-wise constant regularized inversion of the magnetic field. Magn Reson Med 2008;60:1003-9.
50. Kressler B, de Rochefort L, Liu T, et al. Nonlinear regularization for per voxel estimation of magnetic susceptibility distributions from MRI field maps. IEEE Trans Med Imaging 2010;29:273-81.
51. Schofield MA, Zhu Y. Fast phase unwrapping algorithm for interferometric applications. Opt Lett 2003;28:1194-6.
52. Liu T, Khalidov I, de Rochefort L, et al. A novel background field removal method for MRI using projection onto dipole fields (PDF). NMR Biomed 2011;24:1129-36.
53. Tabelow K, Balteau E, Ashburner J, et al. hMRI - A toolbox for quantitative MRI in neuroscience and clinical research. Neuroimage 2019;194:191-210.
54. Weiskopf N, Callaghan MF, Josephs O, et al. Estimating the apparent transverse relaxation time (R2*) from images with different contrasts (ESTATICS) reduces motion artifacts. Front Neurosci 2014;8:278.
55. Zaitsu Y, Kudo K, Terae S, et al. Mapping of cerebral oxygen extraction fraction changes with susceptibility-weighted phase imaging. Radiology 2011;261:930-6.
56. Fan AP, Khalil AA, Fiebach JB, et al. Elevated brain oxygen extraction fraction measured by MRI susceptibility relates to perfusion status in acute ischemic stroke. J Cereb Blood Flow Metab 2020;40:539-51.
57. Hattori N, Bergsneider M, Wu HM, et al. Accuracy of a method using short inhalation of ^{15}O-O_2 for measuring cerebral oxygen extraction fraction with PET in healthy humans. J Nucl Med 2004;45:765-70.
58. Bremmer JP, van Berckel BN, Persoon S, et al. Day-to-day test-retest variability of CBF, $CMRO_2$, and OEF measurements using dynamic 15O PET studies. Mol Imaging Biol 2011;13:759-68.
59. Jain V, Langham MC, Floyd TF, et al. Rapid magnetic resonance measurement of global cerebral metabolic rate of oxygen consumption in humans during rest and hypercapnia. J Cereb Blood Flow Metab 2011;31:1504-12.
60. Miao X, Nayak KS, Wood JC. In vivo validation of T2- and susceptibility-based SvO_2 measurements with jugular vein catheterization under hypoxia and hypercapnia. Magn Reson Med 2019;82:2188-98.
61. Plyavin YA, Blum E. Magnetic parameters of blood cells and high-gradient paramagnetic and diamagnetic phoresis. Magn Gidrodin 1982;19:3-15.
62. Brown R, Cheng Y-CN, Haacke EM, et al. Magnetic resonance imaging: physical principles and sequence design. 2nd ed. Hoboken, NJ: John Wiley & Sons; 2014.

63. Eldeniz C, Binkley MM, Fields M, et al. Bulk volume susceptibility difference between deoxyhemoglobin and oxyhemoglobin for HbA and HbS: a comparative study. Magn Reson Med 2021;85:3383-93.
64. Ishii K, Sasaki M, Kitagaki H, et al. Regional difference in cerebral blood flow and oxidative metabolism in human cortex. J Nucl Med 1996;37:1086-8.
65. Gibbs EL, Gibbs FA, Lennox WG, et al. Regulation of cerebral carbon dioxide. Arch Neur Psych 1942;47:879-89.
66. Olsson E, Wirestam R, Lind E. MRI-based quantification of magnetic susceptibility in gel phantoms: assessment of measurement and calculation accuracy. Radiol Res Pract 2018;2018:6709525.
67. Kennan RP, Zhong J, Gore JC. Intravascular susceptibility contrast mechanisms in tissues. Magn Reson Med 1994;31:9-21.
68. Fernandez-Seara MA, Wehrli FW. Postprocessing technique to correct for background gradients in image-based R2* measurements. Magn Reson Med 2000;44:358-66.
69. Xu Y, Haacke EM. The role of voxel aspect ratio in determining apparent vascular phase behavior in susceptibility weighted imaging. Magn Reson Imaging 2006;24:155-60.
70. Li J, Chang S, Liu T, et al. Phase-corrected bipolar gradients in multi-echo gradient-echo sequences for quantitative susceptibility mapping. Magn Reson Mater Phy 2015;28:347-55.
71. Reichenbach JR, Haacke EM. High-resolution BOLD venographic imaging: a window into brain function. NMR Biomed 2001;14:453-67.
72. Østergaard L. SARS CoV-2 related microvascular damage and symptoms during and after COVID-19: consequences of capillary transit-time changes, tissue hypoxia and inflammation. Physiol Rep 2021;9:e14726.

How to cite this article: Lundberg A, Lind E, Olsson H, Helms G, Knutsson L, Wirestam R. Comparison of MRI methods for measuring whole brain oxygen extraction fraction under different geometric conditions at 7T. J Neuroimaging. 2022;32:442–458. https://doi.org/10.1111/jon.12975